Advances in Nanoparticles, 2025, 14(2), 37-54
https://www.scirp.org/journal/anp
ISSN Online: 2169-0529
ISSN Print: 2169-0510

Prevailing Surface-Controlled Charge Storage Mechanism in Iron Oxcide with Glycine Doping for Supercapacitors

Abubaker Aslam[1], Muhammad Yousaf[2]*, Zeeshan Ahmad[3], Farrukh Saleem Raza[2], Khalilur-Rahman[4], Muhammad Awais Shahid[5], Muhammad Sarwar[6], Muhammad Nazim Hussain[2]

[1]Department of Physics, Government College University Faisalabad, Faisalabad, Pakistan
[2]Department of Physics, University of Agriculture Faisalabad, Faisalabad, Pakistan
[3]Department of Physics, University of Punjab Lahore, Lahore, Pakistan
[4]Department of Physics, Superior University Lahore, Lahore, Pakistan
[5]Department of Physics, University of Lahore, Lahore, Pakistan
[6]Department of Physics, University of Sialkot, Sialkot, Pakistan
Email: abubakeraslam69@gmail.com, *myousafsipra07@mail.com, Za6775858@gmail.com, farrukhsaleemraza@gmail.com, khalil6476473@gmail.com, awaisshahid74@gmail.com, sarmuhammad021@gmail.com, Nazimsandhu123@gmail.com

How to cite this paper: Aslam, A., Yousaf, M., Ahmad, Z., Raza, F.S., Khalilur-Rahman, Shahid, M.A., Sarwar, M. and Hussain, M.N. (2025) Prevailing Surface-Controlled Charge Storage Mechanism in Iron Oxcide with Glycine Doping for Supercapacitors. *Advances in Nanoparticles*, **14**, 37-54.
https://doi.org/10.4236/anp.2025.142003

Received: February 6, 2025
Accepted: March 4, 2025
Published: March 7, 2025

Abstract

Supercapacitors as futuristic types of energy storage devices provide numerous benefits, including high power density, stability, environmentally friendliness, and fast charging and discharging speed. The primary objective of this research is to optimize the charge storage mechanism of Iron Oxcide (Fe_3O_4) nanomaterials with different PVP and glycine concentrations prepared by the sol-gel method. PVP and glycine doping variations the structural characteristics of materials, including modifications in lattice parameters, crystallite size. PVP doping enhances the structural stability and crystallite size of Fe_3O_4, resulting in bigger nanoparticles with a more continuous shape. In contrast, glycine doping dramatically alters the XRD pattern, indicating improved crystallinity, and significantly boosts electrochemical performance. SEM images show the spherical like shape of the pristine and doped Fe_3O_4 nanomaterials. Electrochemical characteristics demonstrate how PYP and glycine doping improve the Fe_3O_4 nanomaterial's effectiveness as an electrode material for supercapacitors. When glycine is doped in Fe_3O_4, the specific capacitance rises to 300 Fg^{-1}, while undoped Fe_3O_4 has 94 Fg^{-1} at a weep rate of 5 mVs^{-1}. Theoretical analyses by employing Dunn's model indicate that surface-controlled mechanisms majorly contributed to the charge storage and portion is as high as 75 % at a sweep rate of 40 mVs^{-1} for glycine doping.

Keywords

Iron Oxide, PVP and Glycine, Sol-Gel Method, Surface Controlled Mechanism, Supercapacitor

1. Introduction

As the global demand for energy continues to rise, the need for efficient, cost-effective, and sustainable energy storage technologies has never been greater [1]. Supercapacitors, with their high power density, fast charge/discharge rates, excellent cycling stability, and low maintenance cost, have emerged as promising candidates for next-generation power devices, complementing traditional energy storage systems like batteries [1]. However, one of the major challenges for supercapacitors is their relatively low energy density, which is typically an order of magnitude lower than that of batteries [2]. The development of new electrode materials with enhanced energy density, without sacrificing power density or cycle life, is essential for advancing supercapacitor performance [3] [4].

Transition metal oxides (TMOs) have gained significant attention in recent years as potential electrode materials for supercapacitors due to their pseudocapacitive behavior and the ability to store energy via faradic redox reactions [5]-[7]. Iron oxide (Fe_xO_γ) nanoparticles, in particular, are highly promising because of their environmental friendliness, low cost, and abundance, which make them attractive for large-scale applications [7] [8]. However, while iron oxide (Fe_3O_4) exhibits excellent stability and conductivity, its low capacitance and poor electron conductivity at high current densities limit its practical applications in supercapacitors [9]-[11].

To overcome these challenges, polymer doping has been explored as an effective strategy for improving the electrochemical properties of iron oxide nanoparticles [12] [13]. For instance, Polyvinylpyrrolidone (PVP) has been used to enhance the structural integrity and stability of iron oxide nanoparticles, thereby improving the electrochemical performance [14]-[16]. Additionally, glycine doping has been investigated as another approach to enhance the electrochemical characteristics of iron oxide by modifying its surface properties and increasing the available active sites for charge storage [17] [18]. Eeu *et al.* [19] synthesized electrodeposited PPy/reduced graphene oxide (rGO)/iron oxide (Fe_2O_3) using a facile one-pot chronoamperometry approach. The specific capacitances are 125.7 and 102.2 Fg^{-1} after 200 cycles at 50 mVs^{-1} scan rate in 1.0 M of KCl electrolyte with capacitive retention at 80.3%. Devi *et al.* [20] investigated Fe_3O_4/rGO nanocomposite by chemical reduction method and achieved a maximum specific capacitance 416 Fg^{-1} at 5 mVs^{-1} with 1 M H_2SO_4 as electrolyte. Bhattacharya *et al.* [21] synthesized Fe_3O_4/rGO nanocomposite using a facile combination of wetchemistry and low-power sonication and exhibited a high specific capacitance of 576 Fg^{-1} at 10 mVs^{-1}. Sagolsem *et al.* [22] Fe_3O_4/rGO/PVP nanocomposite films with different concentrations of Fe_3O_4 were prepared by electrospinning spray process. The minimum value of Ecorr and Icorr was 0.18 V and 4.76 l V, maximum specific capacitances were achieved at 104.12, 169.63 and 124 Fg^{-1} at a current density of 5 Ag^{-1}.

In this study, we present the synthesis of iron oxide (Fe_3O_4 nanoparticles doped with PVP and glycine using the sol-gel method. We aim to investigate how the incorporation of these polymers affects the morphology, crystallinity, and electrochemical performance of the iron oxide nanoparticles. The synthesized nanomaterials were characterized using various techniques, including X-ray diffraction (XRD), scanning electron microscopy (SEM), Fourier-transform infrared (FTIR) spectroscopy, and cyclic voltammetry (CV). The electrochemical properties of the doped and undoped iron oxide nanoparticles were evaluated to assess their potential for supercapacitor applications.

The results show that the doping of PVP and glycine not only enhances the structural stability and surface area of iron oxide but also improves its charge storage capacity, particularly in glycine-doped iron oxide, which exhibits a significantly higher specific capacitance compared to the undoped material. These findings provide insights into the potential of polymer-doped iron oxide nanomaterials for high-performance supercapacitors and contribute to the ongoing development of advanced materials for energy storage applications [23]-[26].

2. Materials

All of the starting raw materials, including $FeCl_3·6H_2O$ [$FeCl_3·6H_2O \geq 98\%$, Sigma Aldrich], $FeCl_2·4H_2O$ [$FeCl_2.4H_2O = 98\%$, Sigma Aldrich, PVP [powder, average M_w ~55,000 Sigma Aldrich], glycine [≥98.5%, suitable for cell culture, non-animal source, meets EP, JP, USP testing specifications], NaOH and DI-Water used for the preparation ma MNPs.

Synthesis

The iron oxide nanoparticles were prepared by using Sol gel method. The ferric chloride hexahydrate ($FeCl_3·6H_2O$) 1 g and ferrous chloride tetrahydrate ($FeCl_2·4H_2O$) 2.2 g were added into deionized water (100 mL). The stirring with the help of magnetic stirrer continued until the iron salt completely dissolved in deionized (DI) water. A specific amount of PVP (50 mL) and glycine (50 mL) is added to the original solution for doping. After that, the temperature was raised on a hot plate up to 75˚C by adding the sodium hydroxide (NaOH 4 g in 10 mL of DI water) solution drop wise in given solution to check the pH (7 - 9) of the solution. After maintaining the pH of samples, for 2:30 hours. The temperature is maintained at 75 ˚C, in this process solution starts changing into gel form. After passing time gel begins to burn slowly, this was an indication of formation of particles successfully. After that the sample is dried properly in Oven for 3 hrs at 90˚C. The dried sample is then converted into fine powder with help of mortar and pestle which is later annealed by furnace at 300˚C to get final sample. Final Samples are ready for characterizations (Schematic **Figure 1**).

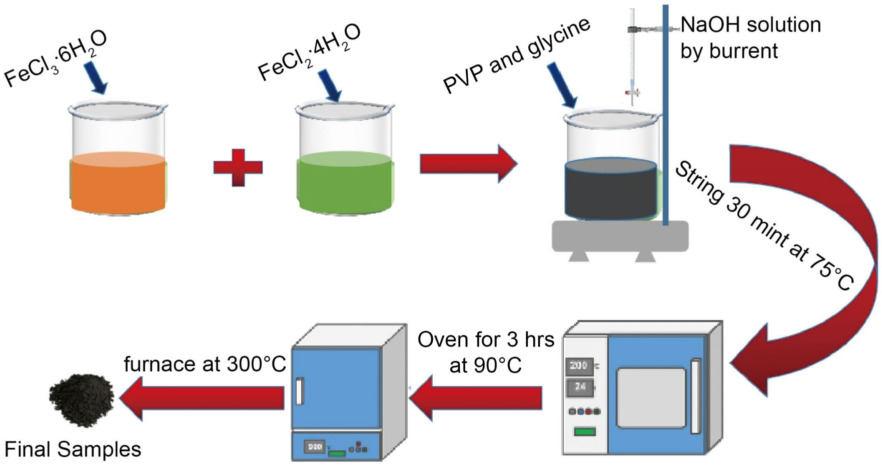

Figure 1. Characterization of the final samples.

Characterization Tool

Various characterization techniques have been used to investigate the properties of synthesized nanomaterials. Structural properties were determined using X-ray diffraction (XRD) with Cu Kα radiation (λ = 0.154 nm). Functional groups were identified by Fourier Transform Infrared Spectroscopy (FTIR) using a Cary 630 spectrophotometer. The optical characteristics of prepared nanomaterials were evaluated by employing a UV–Vis spectrometer (T80). Morphological analysis was performed using scanning electron microscopy (SEM) using a FEI Nova NanoSEM 450.

Working Electrode Fabricated

A working electrode was prepared by mixing graphite, polyvinyl alcohol (binder), and synthetic materials (Fe_3O_4, PVP/Fe_3O_4, glycine/Fe_3O_4) at a ratio of 10:10:80% by weight, respectively. This mixture was then precipitated onto nickel foam. Electrochemical analysis of the fabricated working electrodes was performed in a three-electrode system using 1M KOH electrolyte solution. A platinum (Pt) counter electrode and a Hg/HgO reference electrode were used together with the working electrode, and both were connected to a CS310 workstation.

3. Results and Discussion

XRD is a method for analyzing the structure of generated nanomaterials. The XRD analysis of both pristine and polymer doped Fe_3O_4 are presented in (**Figure 2(a)**). The XRD verifies the rhombohedral structure of iron oxide powder and the generation of single phase Fe_3O_4, which matches the JCPDS card 65 - 3107. The four diffraction peaks are observed at positions 28.94˚, 31.68˚, 45.40˚ and 56.55˚, which correspond to the (220), (311), (411), and (511) planes, respectively [27]. PVP and glycine showed a slight shift as the dopant caused the pristine, but in case of glycine, there is completely shifted at the position of 28.94˚ other ones. In comparison to naked Fe_3O_4 NPs, the polymer doping has also demonstrated impacts on the structural characteristics that differed [28].

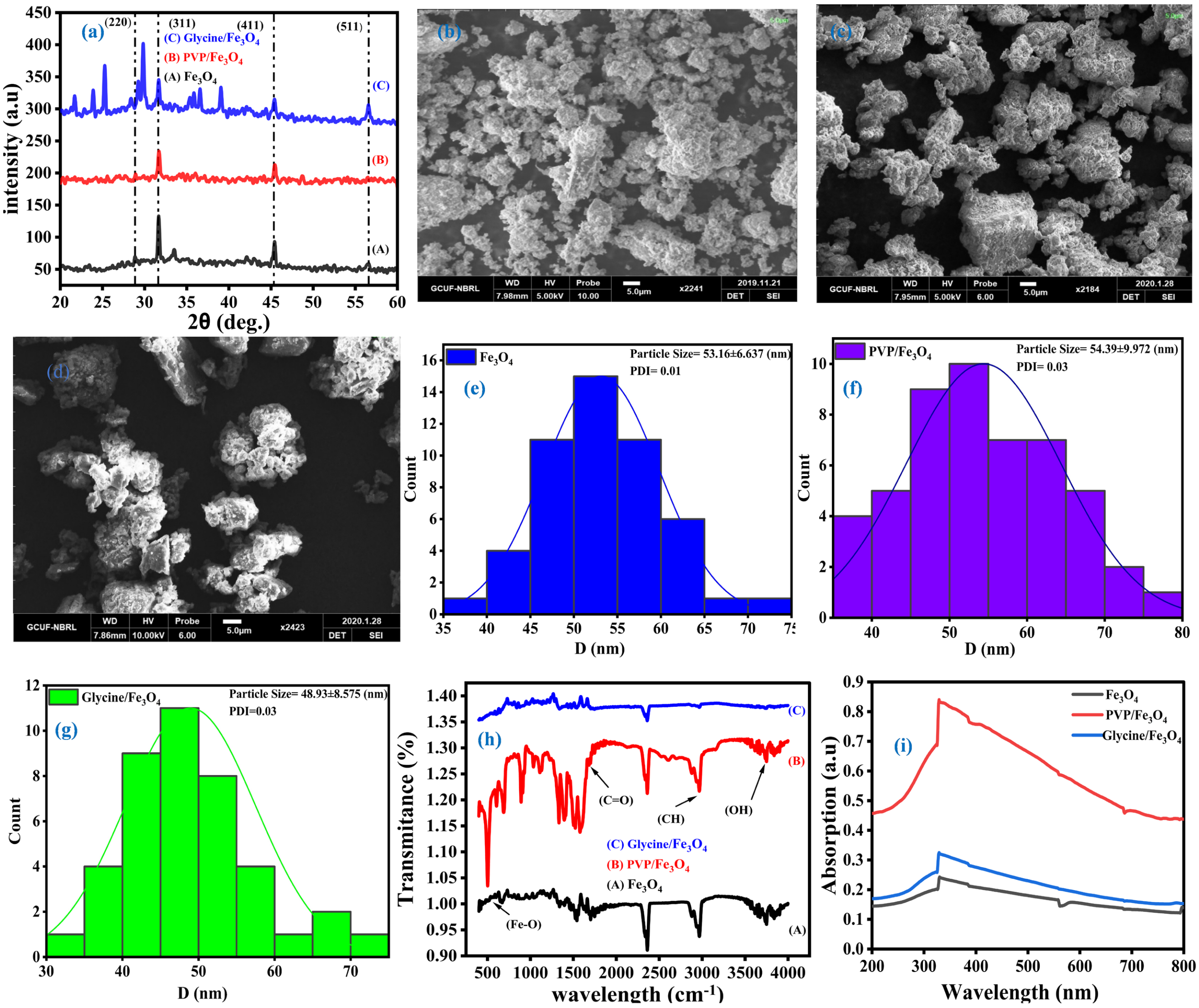

Figure 2. (a) XRD pattern of synthesized Fe_3O_4 and PVP/glycine doped Fe_3O_4 nanomaterials. SEM micrographs and corresponding histograms of (b) Fe_3O_4, (c) PVP/Fe_3O_4, and (d) Glycine/Fe_3O_4 nanomaterials (h) FTIR spectra of Fe_3O_4, PVP/Fe_3O_4, and glycine/Fe_3O_4 nanocomposite materials (i) UV-V is absorption spectrums of synthesized materials.

The average crystal size is determined using Debye-Scherrer's technique, which adheres to Equation (1) [29].

$$D = \frac{k\lambda}{\beta\cos\theta} \tag{1}$$

In this equation where D is crystallite size, k is shape crystal which value is 0.9, shows the wavelength which vale is 1.54 Å, β is FWHM and θ is Bragg's angle. The crystal size of pristine is 12.05 nm, while polymer-doped iron oxide NPs crystallite size is enhanced shown in **Table 1**. So, this might be attributed to the fact that glycine has the largest crystallite size among the dopants [30] [31].

Utilizing a scanning electron microscope, one may examine the grain size and morphology of the nanomaterials. The low and high magnification micrographs of Fe_3O_4 nanoparticles shown in **Figures 2(b)-(d)** show spherical grains with an average size of 53.16 ± 6.637 nm and a 0.01 is the monodisperse index (PDI) value.

Table 1. Comparison of the crystallite size doped and undoped Iron Oxcide.

Sr.No.	Material	Average Size (nm)
1	Iron Oxcide	12.05
2	PVP/Iron Oxcide	22.89
3	Glycine/Iron Oxcide	23.68

A PDI value below 0.1 suggests that the produced NPs are monodispersed [32]. **Figure 2(e)** histogram demonstrates that the bare Fe_3O_4 particles are inside the nano-regime and have a great narrow distribution. When compared to pure Fe_3O_4, the shape of the nanoparticles in PVP/Fe_3O_4 composites varies very little. Spherical particles are visible in the SEM micrographs (**Figure 2(c)**). Nevertheless, the grain size has a tighter size distribution (PDI = 0.03) and is marginally on the upper side, measuring 54.39 ± 9.972 nm. The hybrid form of Fe_3O_4 with PVP is responsible for the increase in particle size because it can encourage the attachment of additional atoms to the particles during the development phase [33]. **Figure 2(d)** displays a mixture of glycine and Fe_3O_4, with a spherical particle shape and an average size of 48.93 ± 8.575 nm. This demonstrates that PVP plays a specific function in the NPs development process, while glycine may simply be combined with Fe_3O_4 without significantly altering the nanomaterials shape.

FTIR spectra of synthesized materials are determined in the range of 500 - 4000 cm^{-1} as shown in (**Figure 2(h)**) highlights the comparison of bare Fe_3O_4, PVP and glycine doped Fe_3O_4 at different peaks. The pattern of PVP doped Fe_3O_4 nanoparticles is similar to the pure Fe_3O_4. But the glycine doped Fe_3O_4 nanoparticles indicated the similar behavior label at four points on the peaks [34]. Various function group existed at the different peaks as shown in **Figure 2(h)**. Moreover, the band of PVP doped Fe_3O_4 NPs was nearly equal to the glycine doped Fe_3O_4 NPs band and little difference absorbance level of both bands [35]. Moreover, the main peak Fe-O is observed in the band at 670 cm^{-1} [36], C=O attached at peak 1701 cm^{-1}, -CH_3 (asymmetric stretching) presented at peak 2967 cm^{-1} [37], and the band at 3745 cm^{-1} belongs to the -OH bond of water molecules adsorbed on the surface of the particles. Many studies reported these higher frequency spectral bands. The same wave number of both spectrums was shown in graph at 1705 cm^{-1} to 3740 cm^{-1} [38].

The UV–Vis absorption spectrum is used to study the optical properties of the synthesized Fe_3O_4, PVP/Fe_3O_4 and glycine/Fe_3O_4 nanomaterials. The bandgap and the type of electronic transitions can be determined from the absorption spectrum. When a semi-conductor absorbs photons of energy larger than the bandgap of the semiconductor, an electron is transferred from the valence band to the conduction band, there occurs an abrupt increase in the absorbance of the material to the wavelength corresponding to the bandgap energy [39]. In **Figure 2(i)**, the absorbance curves of Fe_3O_4, PVP/Fe_3O_4 and glycine/Fe_3O_4 show a peak at 328 nm, 339 nm, and 332 nm respectively. The band gap is determined using Tauc plot method. **Figure S1** shows band gap curves for different materials. The undoped Fe_3O_4 has a band gap of 3.8 eV [18], whereas PVP/Fe_3O_4 and glycine/Fe_3O_4 the band *i.e.* 2.9 eV and 3.2 eV respectively. According to the quantum size effect, the smaller the size of the NPs, the wider the energy bandgap. However, the increase in energy bandgap for doped materials with PVP and glycine indicates that several structural defects are generating allowed states between the valence and conduction band.

4. Electrochemical Analysis

Cyclic Voltammetry (CV)

The electrochemical performance of Fe_3O_4, PVP/Fe_3O_4 and glycine/Fe_3O_4 nanomaterials with different concentrations is determined by CV curves in the potential window range from 0 to 0.45 V. The sweeping speeds of 5 mVs^{-1}, 10 mVs^{-1}, 15 mVs^{-1}, 20 mVs^{-1}, 30 mVs^{-1}, and 40 mVs^{-1} are applied with a three-electrode setup to obtain CV curves. When the scan rate rises from 5 mVs^{-1} to 40 mVs^{-1}, the CV enclosed area expands, indicating fast electron and ion transfer on the prepared electrode surface [40] [41]. The contrast of CV curves for Fe_3O_4 and different concentrations of doped Fe_3O_4 at scan rate of 5 mVs^{-1} is shown in **Figures 3(a)-(c)**. It can be observed that doping increases the peak current and area enclosed in the CV curves as compared to undoped Fe_3O_4 as a first indication of accelerated electrochemical response by PVP and glycine incorporation [42]. When comparing the response of three Fe_3O_4, PVP/Fe_3O_4 and glycine/Fe_3O_4 the oxidation peak current for PVP/Fe_3O_4 higher as compared to glycine/Fe_3O_4 contrarily, the reduction current is the highest in the case of glycine doping [39] [43]. However, for electrochemical performance parameters, the area enclosed by the CV curve is of prime focus along with peak current, and glycine/Fe_3O_4 exhibits a comparatively larger polygonal area at scan rate of 5 mVs^{-1} than undoped and PVP doping material. The slight peak shift can be attributed to the polarization effect [44].

The symmetrical increment in surface area for sweeping at higher scan rates indicates good rate competence, a crucial quality for the actual utilization of supercapacitors. The specific capacitance (Cs) for nanomaterials is calculated by using Equation (4) [45] [46].

$$Cs = \frac{\int_{vc}^{va} I \times \mathrm{d}V}{m \times v \times \Delta V} \tag{2}$$

where m represents the mass of active material, v is scan rate, ΔV potential window and $\int I \times \Delta V$ CV area enclosed. The specific capacitance of Fe_3O_4, PVP/Fe_3O_4 and glycine/Fe_3O_4 are 94 Fg^{-1}, 247 Fg^{-1} and 300 Fg^{-1} respectively at 5 mVs^{-1}.

The Randles-Sevick plot is utilized to estimate the redox contributions. A Randles-Sevick equation is used to illustrate the estimated linear relationship between the current and sweep rate. The graphs of (I_p vs. $\upsilon^{1/2}$) and (I_p vs. υ) present faradic and non-faradic processes in the materials [47]. The linear fitting determines correlation coefficients and the R^2 value indicates the charge storage nature.

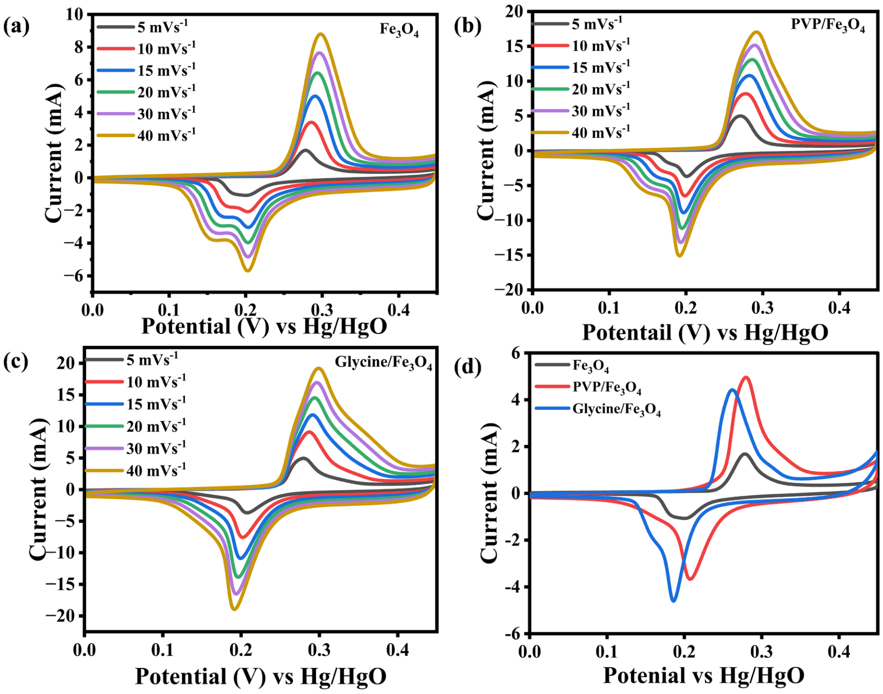

Figure 3. Cyclic voltammetry curves of (a) Fe_3O_4, (b) PVP/Fe_3O_4, and (c) glycine/Fe_3O_4, (d)Comparison of CV curves of all samples at scan rate 5 mV/s.

In each case, inset graph displays the diffusive response, while the main graphs represent the material's capacitive response (**Figures 4(b)-(d)**). For the Fe_3O_4, PVP/Fe_3O_4 and glycine/Fe_3O_4, it can be seen that the charge storage mechanism is mostly due to the surface-controlled process as R^2 is 0.9813, 0.96037, and 0.97816 for respectively. It is seen that the surface-based capacitive response is dominanFe_3O_4, PVP/Fe_3O_4 and glycine/Fe_3O_4 t as compared to the diffusive response (**Figures 4(b)-(d)**).

The electrode's charge storage can follow two ways, a surface-controlled process that happens quite quickly and a slower diffusion-controlled mechanism [47]. The theoretical aspect is also used to determine the ion storage nature of the developed electrodes. The power law (Equations (4-6) has been utilized for this purpose;

$$I_p = a\upsilon^b \tag{3}$$

where I_p is the peak current and ω is the scan rate, and a and b are constants. The b value is used to determine nature of the material *i.e* battery or supercapacitor. When b is equal to 0.5 or 1, there are two different scenarios that apply. If b value is 1, the material can be used as an electrode in supercapacitor (surface-controlled process) and $b = 0.5$ represents the battery-grade materials (diffusion-controlled method). The b value in curve case is 0.8, representing a surface-controlled mechanism or a predominantly capacitive nature of the material as shown in Figure [48]-[50].

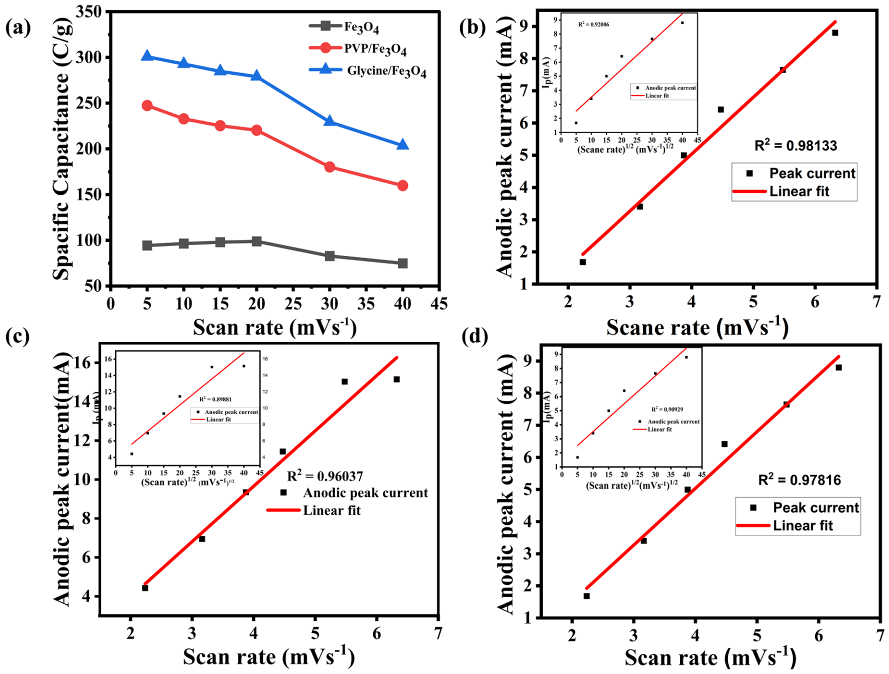

Figure 4. (a) Specifc capacity at different scan rates for all three samples. Capacitive/non-ferodic controlled mechanism differnitiation; I_P vs. υ plot, (inset: I_P vs. $υ^{1/2}$), (b) Fe_3O_4, (c) PVP/Fe_3O_4, and (d) glycine/Fe_3O_4.

Considering the best electrochemical performance of glycine/Fe_3O_4, the b value is determined at various static potentials between 0.23 V and 0.44 V (Figure 5(a)). As the potential rises, the *b* value starts from 0.28 at the lowest potential (0.23 V), increases to 1.11 at 0.35 V, and reduces subsequently (Figure 5(b)). This comparison shows that diffusion process converts generated current linearly into a surface-controlled process as the scan rate increases. Diffusion-controlled mechanism generated by fast intercalation produces the maximum current at peak potentials (ion-exchange process) [50].

Equation (7) is used to elucidate the capacitive and diffusion-controlled effects from the overall charge storage of each electrode,

$$I_p = k_1 v + k_2 v^{1/2} \tag{4}$$

Here, $k_1 v$ and $k_2 v^{1/2}$ represent capacitive and diffusion-limited contributions. We can utilize k_1 and k_2 to find the share of each current contributor (Figure 5(c)). The surface-controlled process is dominated at slow sweep speeds because ions have more time to respond. At faster scan rates, the ions are unable to interact extensively with the electrode surface and consequently have insufficient reaction time [51]. Figure 5(d) shows that the surface-controlled process controls the electrochemi-cal reaction at higher scan rates, while the diffusion-controlled process reduces for glycine/Fe_3O_4. At a scan rate of 40 mVs^{-1}, the Fe_3O_4 exhibits a 38% diffusive contribution and a 62% surface-controlled contribution (Figure S2) and the PVP/Fe_3O_4 shows a 31% diffusive contribution and a 69% surface-controlled con-tribution (Figure S3). However, the capacitive contribution rises to 75% at a scan rate of 40 mVs^{-1} from 52% for glycine/Fe_3O_4. This exhibits the promise of glycine/Fe_3O_4 as an innovative material for future supercapattery applications.

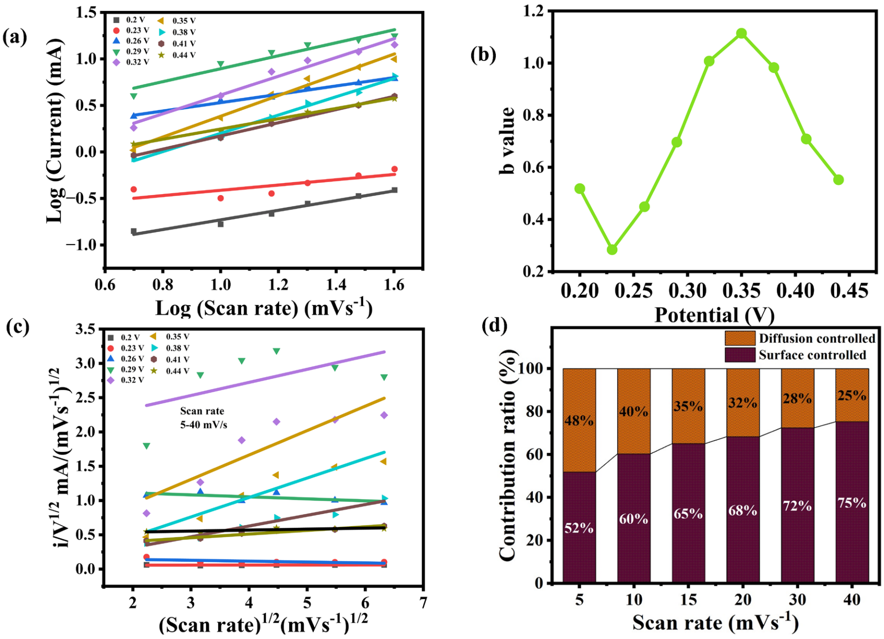

Figure 5. Charge storage mechanism in glycine/Fe_3O_4 (a) Draw a plot at various fixed potentials between the logs of current and scan rate, (b) Change in b at various fixed potentials (c) plot for determining k_1 and k_2, (d) present contribution at various scan rates.

Galvanostatic charge/discharge (GCD)

GCD investigation is used to investigate the electrochemical stored charge mechanism of the fabricated electrodes. Figures 6(a)-(c) shows the GCD curves of Fe_3O_4, PVP/Fe_3O_4, and glycine/Fe_3O_4 at current densities of 1, 3, 7, and 9 Ag^{-1}. The GCD spectra of all electrodes show a quasi-triangular pattern (87 jabir). 10a, b, c. The GCD profile exhibits a non-linear trend (indicated by inflation); of redox reactions

Discharge time decreases with increasing current density. The electrode has the highest capacitance and longest discharge time because it takes the longest time for OH ions to penetrate the electrical contacts at the lowest current density (1 Ag^{-1}). PVP/Fe_3O_4 and glycine/Fe_3O_4 materials take longer to discharge compared to pristine Fe_3O_4, which is also consistent with the CV results

To further explain the distinctive qualities of charge storage, Equation (5) was utilized to calculate the specific capacity (Qs) from GCD measurements:

$$Q_s = \frac{I \times \Delta t}{m} \tag{5}$$

Δt = discharging time, I = current density (A), m = mass loaded. The highest specific capacity is observed for glycine/Fe_3O_4 (301 Cg^{-1}) while the minimum specific capacity (121 Cg^{-1}) is observed for pristine Fe_3O_4 at a current density of 1 Ag^{-1}. Change specific capacity of the various materials according to current density are: **Figures 6(a)-(d)**. The graph shows that glycine/Fe_3O_4 has the highest specific capacity among the three materials. The trend in specific capacity for higher current densities is as follows: Electrochemical bonding between electrolytes because ions and active substances are generated in a short period of time, fast dynamics [52].

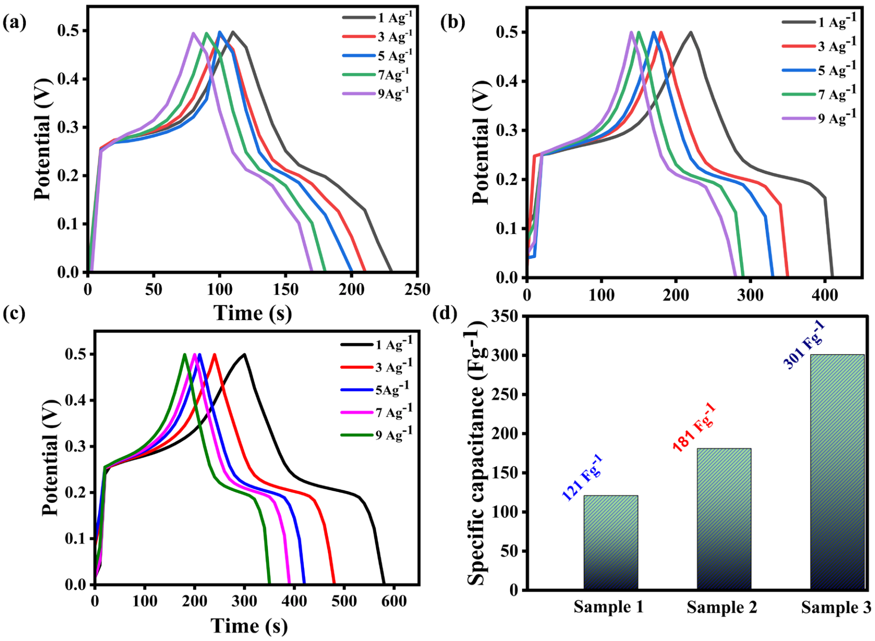

Figure 6. Charge/discharge curves at different current densities: (a) Fe_3O_4, (b) PVP/Fe_3O_4, and (c) glycine/Fe_3O_4, (d) Specific capacity trend at different current densities for different materials.

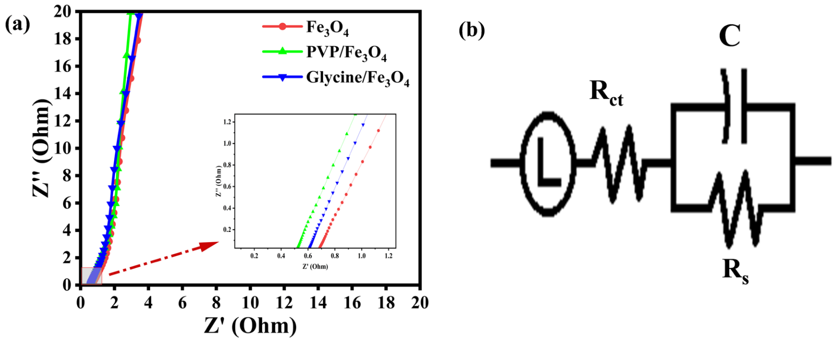

Figure 7. The Nyquist plots comparison of Fe_3O_4, PVP/Fe_3O_4, and glycine/Fe_3O (inset; the high frequency spectra) (b) Equivalent circuit.

Electrochemical impedance spectroscopy (EIS)

EIS analyzes the electron-transport mechanism and conductivity of the produced electrodes in a frequency range of 0.3 Hz to 100 kHz at a voltage of 10 mV. The Nyquist plot displays the behavior of the imaginary and real impedance for (**Figure 7(a)**). The resistance created at the electrolyte-electrode interface during a chemical reaction is known as equivalent series resistance. The Rs values of 0.69

Ω, 0.65 Ω, and 0.52 Ω are obtained for (a) Fe_3O_4, PVP/Fe_3O_4, and glycine/Fe_3O_4, respectively (**Figure 7(b)**). The lowest Rs value glycine/Fe_3O_4 for indicates its enhanced response in electrochemical reactions with ease of electron transfer. The low resistance can help ions transfer into electrically charged materials [53]. The findings support the hypothesis that an electrode modified with glycine/Fe_3O_4 exhibits enhanced electron transfer efficiency. **Figure 7(b)** shows an equivalent circuit. The Rs, Rct, and C represent the solution resistance, charge transfer resistance, and capacitor components, respectively.

5. Conclusion

Fe_3O_4, PVP/Fe_3O_4, and glycine/Fe_3O_4 nanomaterials are efficiently synthesized by using the sol-gel method. Nanomaterials were investigated using the following techniques: XRD, FTIR, and SEM. Fe_3O_4 and PVP/glycine doped Fe_3O_4 nanomaterials illustrated an excellent capacitance effect when applied as supercapacitor electrodes. The Fe_3O_4 material for electrodes has a specific capacitance of 121 Fg^{-1} at a current density of 1 Ag^{-1}. Doping PVP and glycine results in significantly increased electrochemical energy storage capacity. Glycine doped Fe_3O_4 electrodes demonstrated their maximum specific capacitance of 301 Fg^{-1} at a current density of 1 Ag^{-1}, illustrating their electrochemical efficiency. The CV curves illustrate that the surface-controlled method increases with scan rate. At 40 mV/s, there's a surface-controlled mechanism that controls 25% and a diffusion-controlled process that controls 75%. Because of this result, it becomes a special material for future supercapattery purposes.

Conflicts of Interest

The authors declare no conflicts of interest regarding the publication of this paper.

References

[1] Chen, Y., Yao, Y., Zhao, W., Wang, L., Li, H., Zhang, J., *et al.* (2023) Precise Solid-Phase Synthesis of CoFe@FeO_x Nanoparticles for Efficient Polysulfide Regulation in Lithium/Sodium-Sulfur Batteries. *Nature Communications*, **14**, Article No. 7487. https://doi.org/10.1038/s41467-023-42941-9

[2] Yan, J., Wang, Q., Wei, T. and Fan, Z. (2013) Recent Advances in Design and Fabrication of Electrochemical Supercapacitors with High Energy Densities. *Advanced Energy Materials*, **4**, Article ID: 1300816. https://doi.org/10.1002/aenm.201300816

[3] Samuel, E., Joshi, B., Jo, H.S., Kim, Y.I., An, S., Swihart, M.T., *et al.* (2017) Carbon Nanofibers Decorated with Feo Nanoparticles as a Flexible Electrode Material for Symmetric Supercapacitors. *Chemical Engineering Journal*, **328**, 776-784. https://doi.org/10.1016/j.cej.2017.07.063

[4] Zhao, B., Zheng, Y., Ye, F., Deng, X., Xu, X., Liu, M., *et al.* (2015) Multifunctional Iron Oxide Nanoflake/graphene Composites Derived from Mechanochemical Synthesis for Enhanced Lithium Storage and Electrocatalysis. *ACS Applied Materials & Interfaces*, **7**, 14446-14455. https://doi.org/10.1021/acsami.5b03477

[5] Liang, R., Du, Y., Xiao, P., Cheng, J., Yuan, S., Chen, Y., *et al.* (2021) Transition Metal Oxide Electrode Materials for Supercapacitors: A Review of Recent Developments.

Nanomaterials, **11**, Article 1248. https://doi.org/10.3390/nano11051248

[6] Ahmad, F., Shahzad, A., Danish, M., Fatima, M., Adnan, M., Atiq, S., *et al.* (2024) Recent Developments in Transition Metal Oxide-Based Electrode Composites for Supercapacitor Applications. *Journal of Energy Storage*, **81**, Article ID: 110430. https://doi.org/10.1016/j.est.2024.110430

[7] Zhu, X. (2022) Recent Advances of Transition Metal Oxides and Chalcogenides in Pseudo-Capacitors and Hybrid Capacitors: A Review of Structures, Synthetic Strategies, and Mechanism Studies. *Journal of Energy Storage*, **49**, Article ID: 104148. https://doi.org/10.1016/j.est.2022.104148

[8] Zhan, C., Yao, Z., Lu, J., Ma, L., Maroni, V.A., Li, L., *et al.* (2017) Enabling the High Capacity of Lithium-Rich Anti-Fluorite Lithium Iron Oxide by Simultaneous Anionic and Cationic Redox. *Nature Energy*, **2**, 963-971. https://doi.org/10.1038/s41560-017-0043-6

[9] Kumar, R., Nekouei, R.K. and Sahajwalla, V. (2025) In-situ Carbon-Coated Iron Oxide (ISCC-Fe_3O_4) as an Efficient Electrode Material for Supercapacitor Applications. *Ceramics International*. https://doi.org/10.1016/j.ceramint.2025.01.071

[10] Song, H., Wu, M., Tang, X., Liang, J., Zhang, Y., Xie, Y., *et al.* (2025) Synthesis of Fe_3O_4/FeS_2 Composites via MOF-Templated Sulfurization for High-Performance Hybrid Supercapacitors. *Journal of Alloys and Compounds*, **1010**, Article ID: 177658. https://doi.org/10.1016/j.jallcom.2024.177658

[11] Ali, H.G., Khan, K., Hanif, M.B., Khan, M.Z., Hussain, I., Javed, M.S., *et al.* (2023) Advancements in Two-Dimensional Materials as Anodes for Lithium-Ion Batteries: Exploring Composition-Structure-Property Relationships Emerging Trends, and Future Perspective. *Journal of Energy Storage*, **73**, Article ID: 108980. https://doi.org/10.1016/j.est.2023.108980

[12] Arbizzani, C., Mastragostino, M. and Meneghello, L. (1996) Polymer-Based Redox Supercapacitors: A Comparative Study. *Electrochimica Acta*, **41**, 21-26. https://doi.org/10.1016/0013-4686(95)00289-q

[13] Snook, G.A., Kao, P. and Best, A.S. (2011) Conducting-Polymer-Based Supercapacitor Devices and Electrodes. *Journal of Power Sources*, **196**, 1-12. https://doi.org/10.1016/j.jpowsour.2010.06.084

[14] Zhao, Q., Xia, Z., Qian, T., Rong, X., Zhang, M., Dong, Y., *et al.* (2021) PVP-Assisted Synthesis of Ultrafine Transition Metal Oxides Encapsulated in Nitrogen-Doped Carbon Nanofibers as Robust and Flexible Anodes for Sodium-Ion Batteries. *Carbon*, **174**, 325-334. https://doi.org/10.1016/j.carbon.2020.12.016

[15] Zhang, J., Tang, L., Zhang, Y., Li, X., Xu, Q., Liu, H., *et al.* (2021) Polyvinylpyrrolidone Assisted Synthesized Ultra-Small $Na_4Fe_3(PO_4)_2(P_2O_7)$ Particles Embedded in 1D Carbon Nanoribbons with Enhanced Room and Low Temperature Sodium Storage Performance. *Journal of Power Sources*, **498**, Article ID: 229907. https://doi.org/10.1016/j.jpowsour.2021.229907

[16] Durga, I.K., Rao, S.S., Kalla, R.M.N., Ahn, J. and Kim, H. (2020) Facile Synthesis of FeS_2/PVP Composite as High-Performance Electrodes for Supercapacitors. *Journal of Energy Storage*, **28**, Article ID: 101216. https://doi.org/10.1016/j.est.2020.101216

[17] Choi, I., Kwak, D., Han, S., Park, J., Park, H., Ma, K., *et al.* (2017) Doped Porous Carbon Nanostructures as Non-Precious Metal Catalysts Prepared by Amino Acid Glycine for Oxygen Reduction Reaction. *Applied Catalysis B*: *Environmental*, **211**, 235-244. https://doi.org/10.1016/j.apcatb.2017.04.039

[18] Asadi, F., Ahangari, M., Mostafaei, J., Kalantari, N., Delibas, N., Asghari, E., *et al.* (2024) Manganese Doped $La_{0.8}Ba_{0.2}FeO_3$ Perovskite Oxide as an Efficient Electrode

Material for Supercapacitor. *Journal of Alloys and Compounds*, **1004**, Article ID: 175801. https://doi.org/10.1016/j.jallcom.2024.175801

[19] Eeu, Y.C., Lim, H.N., Lim, Y.S., Zakarya, S.A. and Huang, N.M. (2013) Electrodeposition of Polypyrrole/Reduced Graphene Oxide/Iron Oxide Nanocomposite as Supercapacitor Electrode Material. *Journal of Nanomaterials*, **2013**, Article ID: 653890. https://doi.org/10.1155/2013/653890

[20] Nongthombam, S., Aruna Devi, N., Sinha, S., Ishwarchand Singh, W. and Swain, B.P. (2023) Analysis of Structural Defects with the Chemical Composition of rGO/GaN Nanocomposites Using Raman Spectroscopy. *Materials Today*: *Proceedings*, **74**, 744-749. https://doi.org/10.1016/j.matpr.2022.10.302

[21] Bhattacharya, G., Sas, S., Wadhwa, S., Mathur, A., McLaughlin, J. and Roy, S.S. (2017) Aloe Vera Assisted Facile Green Synthesis of Reduced Graphene Oxide for Electrochemical and Dye Removal Applications. *RSC Advances*, **7**, 26680-26688. https://doi.org/10.1039/c7ra02828h

[22] Chanu, S.N., Sinha, S., Devi, P.S., Devi, N.A., Sathe, V., Swain, B.S., *et al.* (2022) Optical, Electrochemical and Corrosion Resistance Properties of Iron Oxide/Reduced Graphene Oxide/Polyvinylpyrrolidone Nanocomposite as Supercapacitor Electrode Material. *Bulletin of Materials Science*, **45**, Article No. 122. https://doi.org/10.1007/s12034-022-02704-6

[23] EL-Ghoul, Y., Alminderej, F.M., Alsubaie, F.M., Alrasheed, R. and Almousa, N.H. (2021) Recent Advances in Functional Polymer Materials for Energy, Water, and Biomedical Applications: A Review. *Polymers*, **13**, Article 4327. https://doi.org/10.3390/polym13244327

[24] Islam, M.R., Afroj, S., Novoselov, K.S. and Karim, N. (2022) Smart Electronic Textile-based Wearable Supercapacitors. *Advanced Science*, **9**, Article ID: 2203856. https://doi.org/10.1002/advs.202203856

[25] Ragab, H.M., Diab, N.S., Aleid, G.M., Alghamdi, A.M., Al-Sagheer, L.A.M. and Farea, M.O. (2024) Enhancement of Structural, Optical, and Electrical Properties of Hydroxypropyl Methylcellulose/Polyvinyl Alcohol Nanocomposites by Nickel Ferrite Nanoparticles for Optoelectronic Applications. *Journal of Inorganic and Organometallic Polymers and Materials*, **35**, 1152-1164. https://doi.org/10.1007/s10904-024-03337-4

[26] Chai, S., Zhang, W., Yang, J., Zhang, L., Theint, M.M., Zhang, X., *et al.* (2023) Sustainability Applications of Rare Earths from Metallurgy, Magnetism, Catalysis, Luminescence to Future Electrochemical Pseudocapacitance Energy Storage. *RSC Sustainability*, **1**, 38-71. https://doi.org/10.1039/d2su00054g

[27] Hsueh, P. (2010) New Delhi Metallo-B-Lactamase-1 (NDM-1): An Emerging Threat among Enterobacteriaceae. *Journal of the Formosan Medical Association*, **109**, 685-687. https://doi.org/10.1016/s0929-6646(10)60111-8

[28] Abbas, F., Jan, T., Iqbal, J., Ahmad, I., Naqvi, M.S.H. and Malik, M. (2015) Facile Synthesis of Ferromagnetic Ni Doped CeO_2 Nanoparticles with Enhanced Anticancer Activity. *Applied Surface Science*, **357**, 931-936. https://doi.org/10.1016/j.apsusc.2015.08.229

[29] Fatimah, S., Ragadhita, R., Husaeni, D.F.A. and Nandiyanto, A.B.D. (2021) How to Calculate Crystallite Size from X-Ray Diffraction (XRD) Using Scherrer Method. *ASEAN Journal of Science and Engineering*, **2**, 65-76. https://doi.org/10.17509/ajse.v2i1.37647

[30] Aisida, S.O., Akpa, P.A., Ahmad, I., Maaza, M. and Ezema, F.I. (2019) Influence of PVA, PVP and PEG Doping on the Optical, Structural, Morphological and Magnetic

Properties of Zinc Ferrite Nanoparticles Produced by Thermal Method. *Physica B: Condensed Matter*, **571**, 130-136. https://doi.org/10.1016/j.physb.2019.07.001

[31] Ahmad, Z. (2023) Surface Morphological Characterization of $Co_{1-x}Ce_xFe_2O_4$ Spinal Ferrites Synthesized by Solide-State Reaction Method. *Advances in Nanoparticles*, **12**, 139-146. https://doi.org/10.4236/anp.2023.123011

[32] Danaei, M., Dehghankhold, M., Ataei, S., Hasanzadeh Davarani, F., Javanmard, R., Dokhani, A., *et al.* (2018) Impact of Particle Size and Polydispersity Index on the Clinical Applications of Lipidic Nanocarrier Systems. *Pharmaceutics*, **10**, Article 57. https://doi.org/10.3390/pharmaceutics10020057

[33] Seo, K., Sinha, K., Novitskaya, E. and Graeve, O.A. (2018) Polyvinylpyrrolidone (PVP) Effects on Iron Oxide Nanoparticle Formation. *Materials Letters*, **215**, 203-206. https://doi.org/10.1016/j.matlet.2017.12.107

[34] Baganizi, D., Nyairo, E., Duncan, S., Singh, S. and Dennis, V. (2017) Interleukin-10 Conjugation to Carboxylated PVP-Coated Silver Nanoparticles for Improved Stability and Therapeutic Efficacy. *Nanomaterials*, **7**, Article 165. https://doi.org/10.3390/nano7070165

[35] Latha, A.A., Anbuchezhiyan, M., Kanakam, C.C. and Selvarani, K. (2017) Synthesis and Characterization of *γ*-Glycine—A Nonlinear Optical Single Crystal for Optoelectronic and Photonic Applications. *Materials Science-Poland*, **35**, 140-150. https://doi.org/10.1515/msp-2017-0031

[36] Lesiak, B., Rangam, N., Jiricek, P., Gordeev, I., Tóth, J., Kövér, L., *et al.* (2019) Surface Study of Fe_3O_4 Nanoparticles Functionalized with Biocompatible Adsorbed Molecules. *Frontiers in Chemistry*, **7**, Article 642. https://doi.org/10.3389/fchem.2019.00642

[37] Zeng, D., Liu, Z., Bai, S. and Wang, J. (2019) Influence of Sealing Treatment on the Corrosion Resistance of PEO Coated Al-Zn-Mg-Cu Alloy in Various Environments. *Coatings*, **9**, Article 867. https://doi.org/10.3390/coatings9120867

[38] Cai, H., An, X., Cui, J., Li, J., Wen, S., Li, K., *et al.* (2013) Facile Hydrothermal Synthesis and Surface Functionalization of Polyethyleneimine-Coated Iron Oxide Nanoparticles for Biomedical Applications. *ACS Applied Materials & Interfaces*, **5**, 1722-1731. https://doi.org/10.1021/am302883m

[39] Cai, J., Zhou, Q., Gong, X., Liu, B., Zhang, Y., Dai, Y., *et al.* (2020) Metal-Free Amino Acid Glycine-Derived Nitrogen-Doped Carbon Aerogel with Superhigh Surface Area for Highly Efficient Zn-Air Batteries. *Carbon*, **167**, 75-84. https://doi.org/10.1016/j.carbon.2020.06.002

[40] Xing, L., Huang, K., Cao, S. and Pang, H. (2018) Chestnut Shell-Like $Li_4Ti_5O_{12}$ Hollow Spheres for High-Performance Aqueous Asymmetric Supercapacitors. *Chemical Engineering Journal*, **332**, 253-259. https://doi.org/10.1016/j.cej.2017.09.084

[41] O'Neill, L., Johnston, C. and Grant, P.S. (2015) Enhancing the Supercapacitor Behaviour of Novel Fe_3O_4/FeOOH Nanowire Hybrid Electrodes in Aqueous Electrolytes. *Journal of Power Sources*, **274**, 907-915. https://doi.org/10.1016/j.jpowsour.2014.09.151

[42] Liu, M., Yu, Y., Liu, B., Liu, L., Lv, H. and Chen, A. (2018) PVP-Assisted Synthesis of Nitrogen-Doped Hollow Carbon Spheres for Supercapacitors. *Journal of Alloys and Compounds*, **768**, 42-48. https://doi.org/10.1016/j.jallcom.2018.07.234

[43] AlFawaz, A., Ahmad, A., Ahmad, N. and Alharthi, F.A. (2022) Glycine Based Auto-Combustion Synthesis of ZnO Nanoparticles as Electrode Material for Supercapacitor. *Physica Scripta*, **97**, Article ID: 030009. https://doi.org/10.1088/1402-4896/ac52f8

[44] Du, J., Chen, A., Zhang, Y., Zong, S., Wu, H. and Liu, L. (2020) PVP-Assisted Prepa-

ration of Nitrogen Doped Mesoporous Carbon Materials for Supercapacitors. *Journal of Materials Science & Technology*, **58**, 197-204. https://doi.org/10.1016/j.jmst.2020.02.088

[45] Alqarni, A.N., Cevik, E., Gondal, M.A., Almessiere, M.A., Baykal, A., Bozkurt, A., *et al.* (2022) Synthesis and Design of Vanadium Intercalated Spinal Ferrite ($Co_{0.5}Ni_{0.5}V_xFe_{1.6-x}O_4$) Electrodes for High Current Supercapacitor Applications. *Journal of Energy Storage*, **51**, Article ID: 104357. https://doi.org/10.1016/j.est.2022.104357

[46] Peng, C., Zhang, S., Jewell, D. and Chen, G.Z. (2008) Carbon Nanotube and Conducting Polymer Composites for Supercapacitors. *Progress in Natural Science*, **18**, 777-788. https://doi.org/10.1016/j.pnsc.2008.03.002

[47] Mathis, T.S., Kurra, N., Wang, X., Pinto, D., Simon, P. and Gogotsi, Y. (2019) Energy Storage Data Reporting in Perspective—Guidelines for Interpreting the Performance of Electrochemical Energy Storage Systems. *Advanced Energy Materials*, **9**, Article ID: 1902007. https://doi.org/10.1002/aenm.201902007

[48] Kurra, N., Alhabeb, M., Maleski, K., Wang, C., Alshareef, H.N. and Gogotsi, Y. (2018) Bistacked Titanium Carbide (MXene) Anodes for Hybrid Sodium-Ion Capacitors. *ACS Energy Letters*, **3**, 2094-2100. https://doi.org/10.1021/acsenergylett.8b01062

[49] Wang, J., Polleux, J., Lim, J. and Dunn, B. (2007) Pseudocapacitive Contributions to Electrochemical Energy Storage in TiO_2 (Anatase) Nanoparticles. *The Journal of Physical Chemistry C*, **111**, 14925-14931. https://doi.org/10.1021/jp074464w

[50] Sathiya, M., Prakash, A.S., Ramesha, K., Tarascon, J. and Shukla, A.K. (2011) V_2O_5-Anchored Carbon Nanotubes for Enhanced Electrochemical Energy Storage. *Journal of the American Chemical Society*, **133**, 16291-16299. https://doi.org/10.1021/ja207285b

[51] Iqbal, M.Z., Siddique, S., Shaheen, M., Alam, S. and Alzaid, M. (2022) Role of Ag and Cu as an Interfacial Layer on the Electrochemical Performance of $Ni/Ag/Co_3(PO_4)_2$ and $Ni/Cu/Co_3(PO_4)_2$ Electrodes for Hybrid Energy Storage Devices. *Ceramics International*, **48**, 15686-15694. https://doi.org/10.1016/j.ceramint.2022.02.103

[52] Iqbal, M.Z., Abbasi, U. and Alzaid, M. (2022) Cobalt Manganese Phosphate and Sulfide Electrode Materials for Potential Applications of Battery-Supercapacitor Hybrid Devices. *Journal of Energy Storage*, **50**, Article ID: 104632. https://doi.org/10.1016/j.est.2022.104632

[53] Noori, A., El-Kady, M.F., Rahmanifar, M.S., Kaner, R.B. and Mousavi, M.F. (2019) Towards Establishing Standard Performance Metrics for Batteries, Supercapacitors and Beyond. *Chemical Society Reviews*, **48**, 1272-1341. https://doi.org/10.1039/c8cs00581h

Appendix

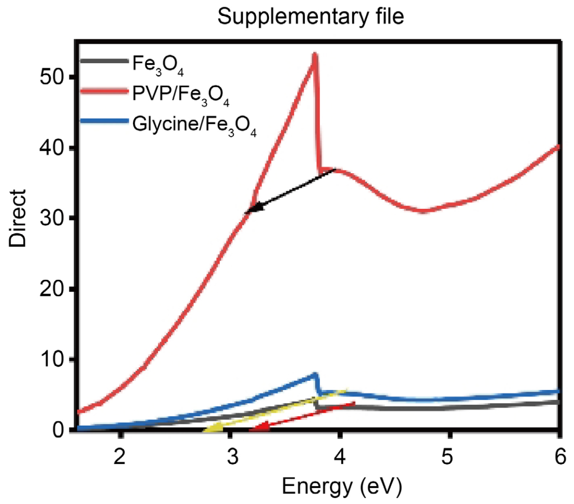

Figure S1. Band gap by UV-visible.

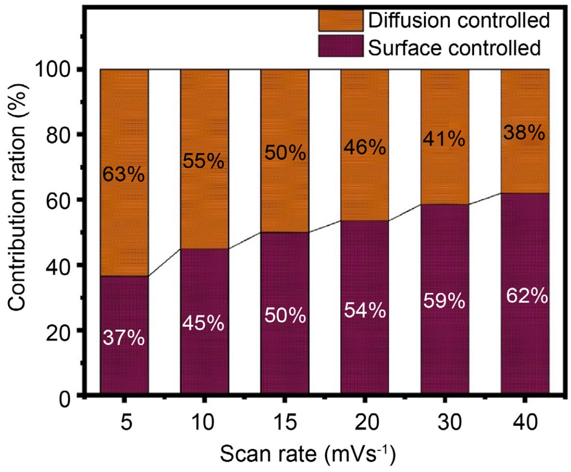

Figure S2. Contribution of Fe$_3$O$_4$.

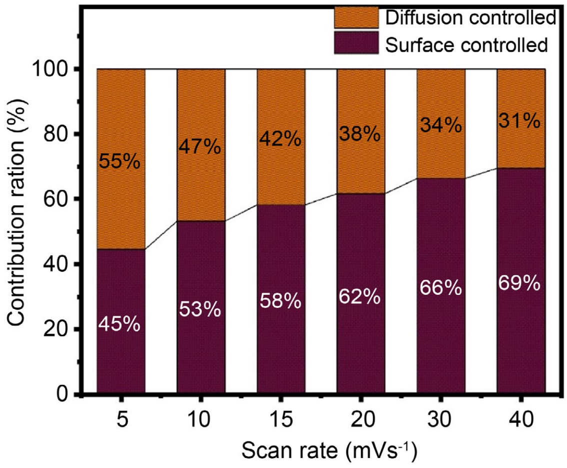

Figure S3. Contribution PVP/Fe$_3$O$_4$.